

Optimization of 3D Printing Parameters for Alumina Ceramic Based on the Orthogonal Test

Shuo Wang, Yongsheng Xiang, Hui Feng, Yanjun Cui,* Xiaofei Liu, Xiaoxin Chang,* Jinxiu Guo, and Peng Tu



Cite This: *ACS Omega* 2024, 9, 16734–16742



Read Online

ACCESS |

Metrics & More

Article Recommendations

ABSTRACT: In this paper, an alumina ink with good rheological properties was successfully prepared using pseudoboehmite as the main component, nitric acid as the colloidal solvent, and sesbania powder as the lubricant. The impact of nine different ink formulations, namely, Ink1 to Ink9, on the printability and rheological features of the ink was investigated. Consequently, it was found that Ink3 with 5 wt % nitric acid and 5 wt % sesbania powder exhibited the most favorable formability. This ink was utilized to fabricate alumina samples with direct ink writing (DIW) three-dimensional (3D) printing technology. The printed alumina samples were characterized using an automatic Brunauer–Emmett–Teller, X-ray diffractometer, Fourier transform infrared spectroscopy, and scanning electron microscope. To obtain the optimal printing parameters, a three-factor and three-level orthogonal test was designed to research the influences of different 3D printing parameters (filling ratio, nozzle diameter, and layer thickness) on the specific surface area, pore characteristics (size and volume), and radial crushing strength of the alumina specimens. The primary and secondary orders of the effects on the radial crushing strength and pore structure were determined through analysis of the experimental data. The experimental results showed that the alumina sample with a filling ratio of 80%, nozzle diameter of 0.6 mm, and layer thickness of 0.3 mm was found to have better strength of 48.07 ± 9.53 N/mm and specific surface area of 185.7315 m²/g. This study provides a theoretical base for the preparation of alumina carriers by DIW 3D printing.



INTRODUCTION

Alumina (Al₂O₃) is the most widely used catalyst carrier in industry, accounting for approximately 70% of industrially supported catalysts. Pseudoboehmite is the main raw material to prepare alumina carriers. Pseudoboehmite exhibits several unique properties, such as large specific surface area, large pores, a spatial network structure, and the ability to transform into viscous colloids under acidic conditions. Shaping is a crucial step in the preparation of catalysts at the industrial scale, and the shaping processes utilized for pseudoboehmite primarily include kneading-extrusion,¹ drop-solidification,^{2–5} and rotational granulation.⁶ However, the catalyst carriers produced through these shaping methods typically exhibit conventional morphologies such as strips, spheres, rings, trilobes, and honeycombs. These catalyst carriers may not fulfill the requirements of certain reactions that necessitate high mass-transfer efficiency or processes that demand the use of integral catalysts.

Recently, three-dimensional (3D) printing is a rapid prototyping technology to build an object layer by layer, which is called additive manufacturing as well. A 3D printing technology can direct the design of structures through computer-aided modeling and easy adaptation to product

requirements by changing model designs and printer parameters, which is difficult to achieve by traditional technology.⁷ It has gained increasing attention in recent years.^{8–10} The 3D printing techniques for ceramics mainly include direct ink writing (DIW),¹¹ selective laser sintering,¹² stereolithography appearance,¹³ and digital light processing.¹⁴

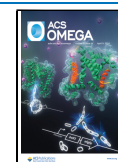
DIW is a technique that involves preparing ink with a mixture of powder, binder, and solvent and then pressing the ink out of the nozzle by using pneumatic pressure, so that it enables the deposition of material in sequential layers, resulting in the formation of a 3D integrated structure. This technique has advantages in material compatibility, precision, and process maturity, making it possible to design and produce materials with internal structures and complex shapes.^{15,16} Material compatibility is a unique feature of DIW. It can be utilized for creating structures using a variety of materials, involving

Received: January 24, 2024

Revised: February 27, 2024

Accepted: March 12, 2024

Published: March 26, 2024



ceramics,¹⁷ polymers,¹⁸ food,¹⁹ metal composites,²⁰ and more. For forming ceramic structures through the DIW process, a focal point is designing an ink with flowable viscoelastic that can be extruded from various types of nozzles and stacked to construct a 3D shape. The compositions of the ink and the critical printing parameters have the greatest effect on the printed specimen. In the past few years, researchers have done a lot of research to develop material through DIW, especially for alumina. Desirable ink design and optimization of printing parameters were studied by many researchers.^{21,22} Although previous research has investigated the mechanical properties or other properties of alumina, studies on the effect of printing parameters on the product performance during the DIW process are still not complete. Additionally, it remains unclear which specific printing parameter has the greatest influence among the factors considered. Currently, there has been a lot of research about using alumina powder to prepare monolithic ceramics by the DIW process. Liu et al.²³ reported the method of preparing ceramics by DIW with a formula of alumina ink involves little organic additives, and finally dense and complicated ceramics were prepared. Yang et al.²⁴ proposed a new 3D printing technology of alumina ceramic parts based on thermally induced DIW and successfully used alumina powder to prepare nonporous thin-walled alumina ceramics with complex shapes. However, there are few reports about using pseudoboehmite to prepare γ -Al₂O₃ for the catalytic carrier.

In this study, inks suitable for the DIW process were prepared by using pseudoboehmite alumina powder as the main component, nitric acid as the colloid solvent, and sesbania powder as the lubricant. Rheological characteristics and the printability of different alumina ceramic inks were investigated. To explore the impact of layer thickness, filling ratio, and nozzle diameter on the properties of printed alumina, nine specimens were prepared using a three-factor and three-level orthogonal table. According to the analysis of experimental results, an optimal printing parameter for an alumina ceramic is obtained.

MATERIALS AND METHODS

Materials. Pseudoboehmite powder (Sasol, Germany) was used as a precursor material. Sesbania powder (Beijing General Research Institute of Mining & Metallurgy Technology Group, China) was added into alumina suspension for lubrication. The nitric acid (65.0–68.0%, Sichuan Xilong Scientific Co., Ltd., China) was used as the peptizer solvent.

Alumina Ink Preparation. To prepare alumina ink for DIW process, sesbania powder and pseudoboehmite powder were weighed and then mixed with deionized water and nitric acid. To improve the accuracy of weighing, sesbania powder and pseudoboehmite powder need to be dried before weighing. During the experiment, sesbania powder and pseudoboehmite powder were mixed evenly, and then the mixed powder was fully dissolved in deionized water, and nitric acid was added dropwise while stirring. Stirring was done at room temperature for 10 min to obtain uniform gel ink.

DIW and Postheat Treatment Process. In this experiment, a 3D printer (CC3003D printer, Shannxi Fiber-Cerachem Technology Development Co., Ltd.) was utilized for sample preparation. Alumina ink, packed in a plastic bucket, was extruded by using an air compressor at a pressure ranging from 0.3 to 0.4 MPa. The rotation of the screw facilitated ink flow smoothly through the nozzle, forming a continuous thin

line. Layer-by-layer deposition enabled the formation of 3D alumina parts. The 3D models of the alumina parts were designed using SolidWorks software (as shown in Figure 1).

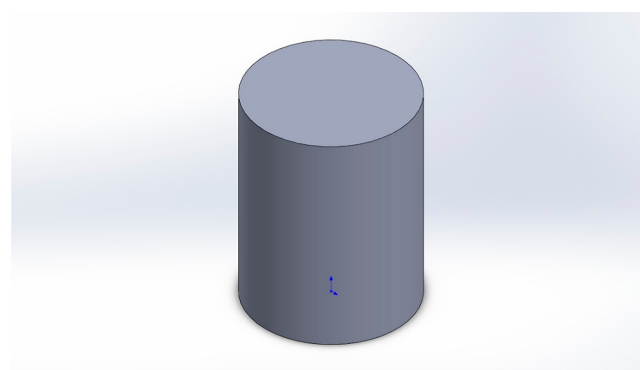


Figure 1. Model diagram of the sample.

Subsequently, Simplify3D software was employed to design the printing parameters, which were converted to G codes and transferred to the 3D printer to print. All models were scaled up at a ratio of 1:1.67, and the samples were printed by cross-stacking at a printing speed of 2000 mm/min. During the experiment, the addition ratio of materials was optimized to investigate the impact of the compositions of the alumina ink on the printing formability. The mechanical properties and pore structure of alumina specimens with different printing parameters, including filling rate (A), nozzle diameter (B), and layer thickness (C), were tested and compared by designing three factors and three levels orthogonal experiments. According to the three factors and three levels, orthogonal experiments were carried out, and nine groups of cylindrical parts were prepared whose height and bottom diameter are all 10 mm.

The alumina green body was placed at room temperature for about 12 h to solidify after printing and then put in the oven to dry at 110 °C for 6 h. At last, the dried alumina green body was put into a muffle furnace for sintering. In order to obtain γ -Al₂O₃ which can be used as a catalyst carrier, the specimen was heated up to 600 °C in 2 h and sintered at 600 °C for 5 h. Finally, the sample was cooled to room temperature after sintering. The print sample preparation scheme is provided in Figure 2.

Characterization and Analysis Methods. In order to obtain the influence of printing ink composition on rheological properties, experiments were carried out on printing inks with different compositions with an intelligent rotary rheometer (Anton Paar Shanghai Trading Co., Ltd.) equipped with a 25 mm diameter parallel plate (PP25). The shear rate was increased from 0.01 to 100 s⁻¹ in the viscosity curve experiment. Storage modulus (*G'*) and loss modulus (*G''*) were measured by amplitude scanning, and the scanning range was 0.1–10,000% at the frequency of 1 Hz. The radial crushing strength of alumina samples was carried out according to ASTM D6175 measured by a particle size strength tester (HB-KQD, Jinan Haibo Laboratory Instrument Co., Ltd., China). The samples were characterized by an X-ray polycrystal diffractometer (MSAL XD-3, Beijing General Analytical Instrument Co., Ltd., China). The tube voltage was 40 kV, the tube current was 30 mA, the scanning rate was 2°/min, and the angle scanning range was 10–80°. A Fourier infrared spectrometer (FTIR-650, Tianjin Gangdong SCI.&TECH.

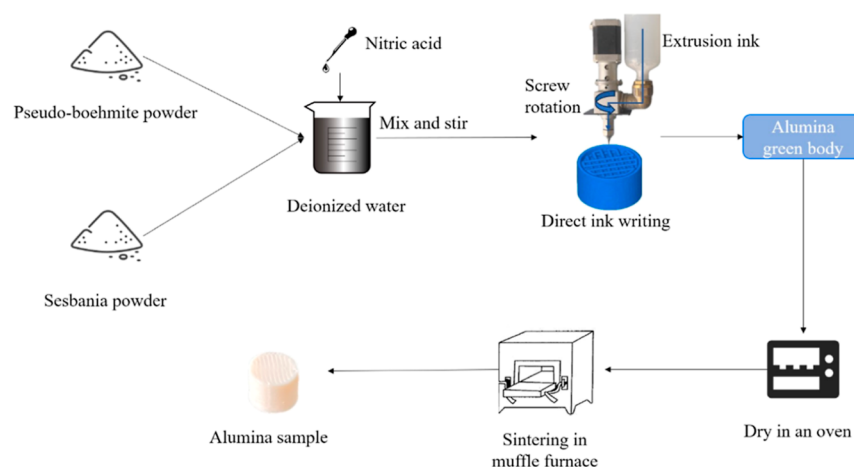


Figure 2. Process of preparing alumina by DIW.

Co., Ltd., China) was used to measure the infrared spectrum of the samples. Before the test, the samples were needed to be dried, and the scanning range of wavenumber was set to 400–4000 cm^{-1} . The pore characteristics, including pore volume, pore size distribution, and specific surface area, were determined using an automatic specific surface area and porosity analyzer (TStar II 3020HD, Micromeritics Instruments Corporation, USA). Scanning electron microscopy (SEM, Phenom G6, China) was used to observe the morphology of each sample at a 5 kV accelerating voltage.

RESULTS AND DISCUSSION

Printability of Alumina Ink. In DIW, the word “printability” includes two concepts, namely, great extrudability and accurate appearance fidelity.²⁵ The composition of the ink solvents plays a vital role in developing high-quality ceramics. The study focuses on two key factors, the addition of sesbania powder and utilization of nitric acid, to achieve the desired alumina monomer. The compositions of alumina ink are presented in Table 1. Compared to samples of Ink-2 and Ink-3

Table 1. Composition of the Alumina Ink^a

sample	R1 (m_1/m)	R2 (m_2/m)	R3 (m_3/m)
Ink-1	0.05	0.04	1.65
Ink-2	0.05	0.045	1.65
Ink-3	0.05	0.05	1.65
Ink-4	0.05	0.055	1.65
Ink-5	0.05	0.06	1.65
Ink-6	0	0.05	1.65
Ink-7	0.01	0.05	1.65
Ink-8	0.03	0.05	1.65
Ink-9	0.07	0.05	1.65

^a m : mass of pseudoboehmite powder, m_1 : mass of sesbania, m_2 : mass of nitric acid, and m_3 : mass of deionized water.

(as depicted in Figure 3b,c), the samples of Ink-1, Ink-4, and Ink-5 (as shown in Figure 3a,d,e) exhibited defects due to insufficient self-supporting force. This is mainly because there are many hydroxyl groups on the surface of pseudoboehmite microcrystals, which have high activity. H^+ ions in nitric acid react with these hydroxyl groups and adsorb on pseudoboehmite particles to form new particles. Under stirring, the new particles continuously adsorb other pseudoboehmite particles. A plurality of pseudoboehmite particles are connected together

in the form of a net by H^+ ions, so that the particles lose fluidity and become colloidal. However, the Ink-1 sample had a low concentration of nitric acid, the acidic peptization of pseudoboehmite particles was insufficient, the binding force between particles was weak, and the fluidity of sol was strong, so it was difficult to form a stable gel. Consequently, the printed samples lacked a sufficient strength. On the other hand, Ink-4 and Ink-5 had relatively higher nitric acid concentrations. As a result of excessive acidification of pseudoboehmite powder, the internal stress of the powder increased, and the degree of aggregation of sol was higher. So that the extruded lines were easy to deform and agglomerate, and it was difficult to form continuous lines, which made it difficult to print and shape samples. In order to reduce the friction between material particles and between material and equipment and then improve the extrusion speed, it is necessary to add a certain proportion of sesbania powder as a lubricant to the raw material powder. With the increase in sesbania powder content, Ink-6, Ink-7, and Ink-8 were successfully printed and formed (as seen in Figure 3f,g,h). However, samples printed with Ink-9, which had the highest sesbania powder content, could not be formed (Figure 3i). This was primarily because the higher content of sesbania powder caused the ink particles to aggregate easily. In addition, it was found that the surfaces of sample printed by Ink-6 and Ink-7 were not completely filled compared with Ink-3, mainly because the lines were difficult to extrude because of the low content of sesbania powder.

Compared with Ink-3, Ink-8 had a higher content of sesbania powder, and the sesbania powder was burned out in the postheat treatment process, which led to the loose structure of the sample and was more prone to fracture (as shown in Figure 4a). On the other hand, the printability and strength of samples printed with Ink-2 and Ink-3 (as shown in Figure 4b,c) were better than those printed with other inks, and the lines of the samples printed with Ink-3 were more complete and uniform (as shown in Figure 4d).

Rheological Behaviors of Alumina Ink. The rheological properties of printing ink decided whether it could be successfully printed and formed through the DIW process.²⁶ As shown in Figure 5, as the shear rate increases, printing ink showed a downward trend in viscosity. This phenomenon was shear thinning, indicating that the alumina ink was a non-Newtonian fluid.^{11,27,28} Consequently, the printing ink can be

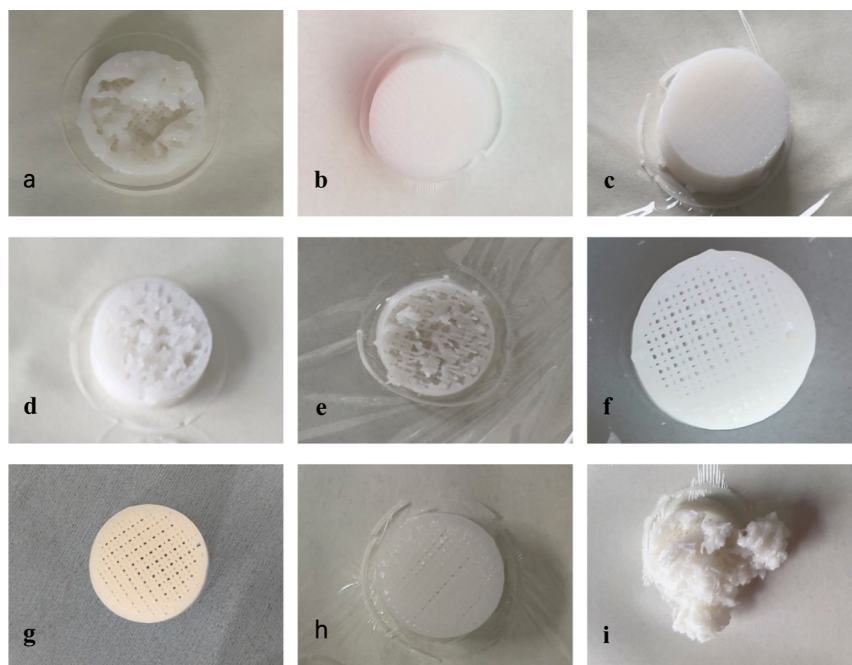


Figure 3. Samples printed with different alumina inks: (a) Ink-1, (b) Ink-2, (c) Ink-3, (d) Ink-4, (e) Ink-5, (f) Ink-6, (g) Ink-7, (h) Ink-8, and (i) Ink-9.

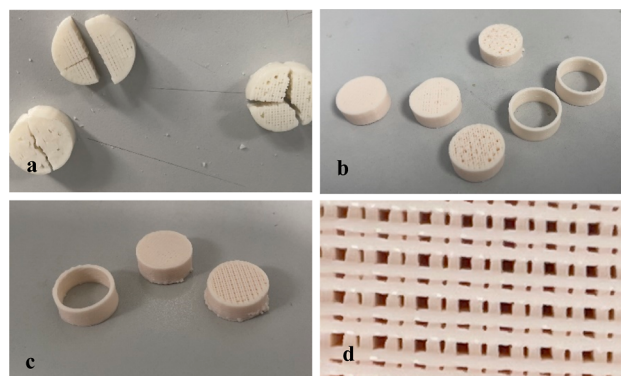


Figure 4. Samples printed with different alumina inks after the postheat treatment process: (a) Ink-8, (b) Ink-2, and (c,d) Ink-3.

squeezed out easily by rotational shearing of the printer screw during the DIW process.

Figure 6 illustrates the connection between the modulus (G' and G'') and shear stress of various alumina inks. Storage modulus (G') exceeds loss modulus (G'') at low shear stress, indicating a linear viscoelastic region. Ink-3, Ink-2, and Ink-6 displayed relatively high storage moduli (in the range 27,362–38,261 Pa) at low shear stress, providing sufficient strength to support the upper layers during the printing process, ensuring smooth molding. With the increases of shear stress, the loss modulus curve and storage modulus curve cross at a specific point, enabling determination of the yield stress (τ_y) at this point. At this stage, the ink exhibits characteristics of both a liquid and a solid. Compared to Ink-3, Ink-2, and Ink-6, the other inks had lower yield stresses (τ_y), implying that they more easily reached the flow point at lower shear stresses. However, due to their lower storage modulus and inadequate self-supporting ability, samples printed with these inks face

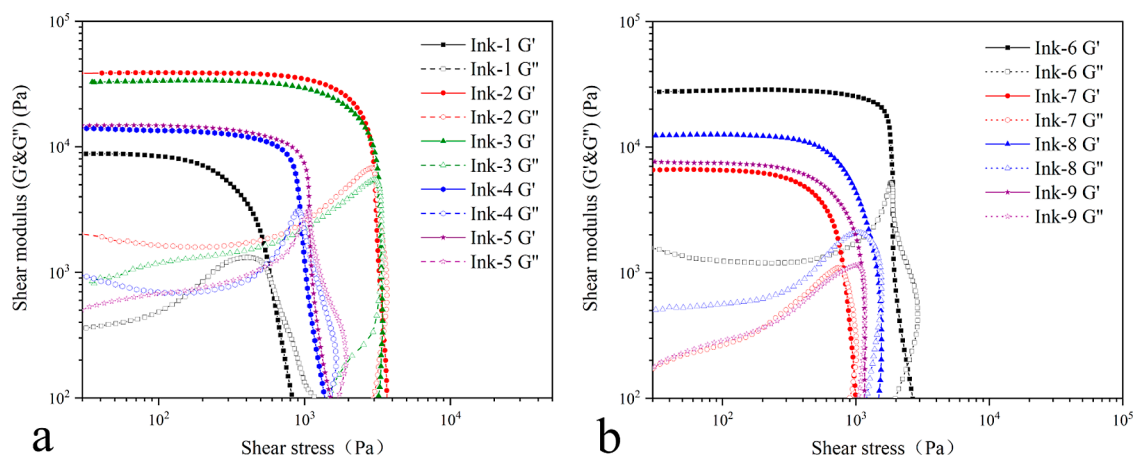


Figure 5. Relationship between viscosity and shear rate of alumina ink: (a) different nitric acid content and (b) different sesbania powder content.

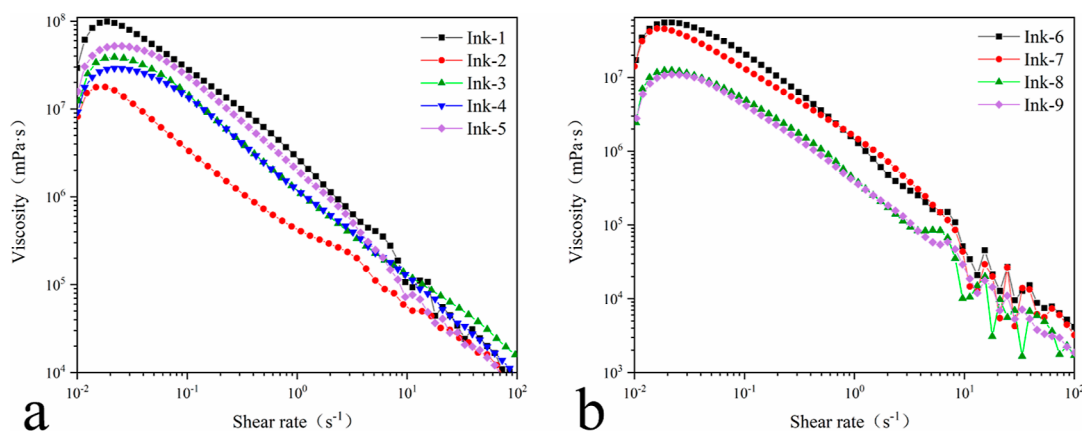


Figure 6. Relationship between storage modulus (G'), loss modulus (G''), and shear stress of alumina ink: (a) different nitric acid content and (b) different sesbania powder content.

difficulties in forming.²⁸ Therefore, Ink-3, Ink-2, and Ink-6 demonstrated better printability with the sample printed using Ink-3 showing the optimal results.

Characterization of the 3D Printed Alumina. The printed samples, produced using the optimal alumina ink known as Ink3, were characterized after sintering at 600 °C by using X-ray diffraction (XRD) and Fourier transform infrared spectroscopy. Figure 7 displays the XRD pattern. As clearly

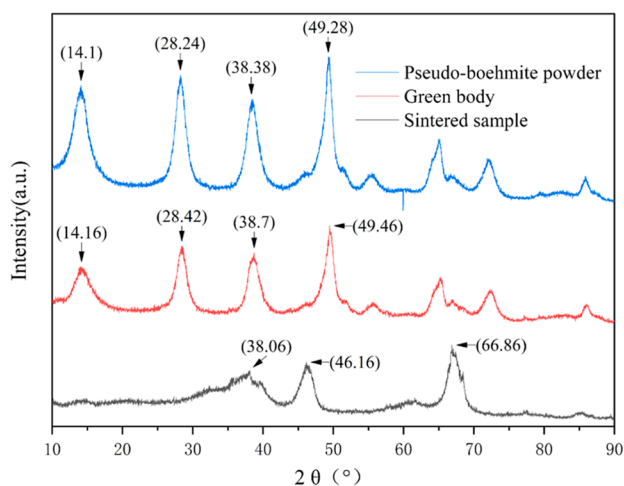


Figure 7. XRD patterns of pseudoboehmite powder and sintered sample.

shown in the figure, the pseudoboehmite powder before molding exhibited prominent diffraction peaks at $2\theta = 14.1$, 28.24, 38.38, and 49.28°, which are typical characteristic peaks of the α' -AlOOH phase. In contrast, there is no obvious difference in diffraction peaks between the printed green body and pseudoboehmite powder, which indicates that no other phases appear during mixing and printing. Besides, the specimen sintered at 600 °C displayed diffraction peaks at $2\theta = 38.06$, 46.16, and 66.86°, indicating that the printed alumina sample transformed from the α' -AlOOH phase to the γ -Al₂O₃ phase after sintering.²⁹ The γ -Al₂O₃ belongs to activated alumina, which possesses good adsorption performance and high-temperature resistance, making it suitable for applications as adsorbents, dehydrating agents, catalysts, and carriers.

Figure 8 shows the IR spectrum. The absorption peaks of raw materials caused by the stretching vibration of the –OH

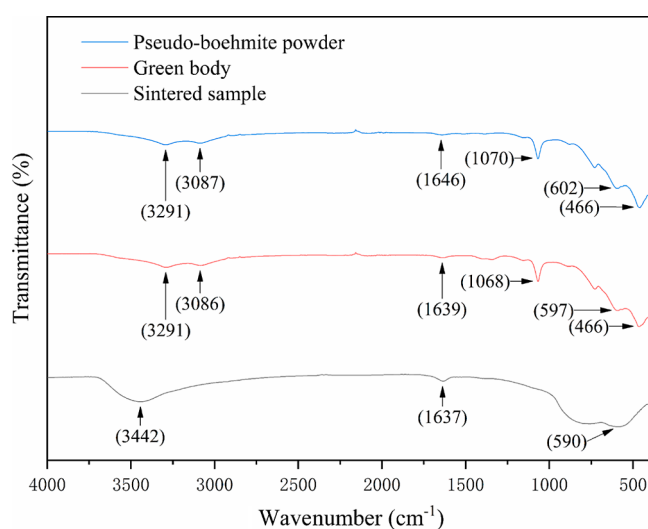


Figure 8. Infrared spectrum patterns of pseudoboehmite powder and sintered sample.

group appeared at 3291 and 3087 cm^{-1} . The peak at 1646 cm^{-1} is due to the deformation vibration of adsorbed and bound water molecules. Additionally, there was a peak at 1070 cm^{-1} attributed to C–O, and the peaks are ascribed to Al–O at 602 and 466 cm^{-1} . These absorption peaks, which belong to raw materials, correspond to the characteristic peaks of pseudoboehmite. There is no obvious difference between the characteristic peaks of the printed green body and pseudoboehmite powder, indicating that no chemical reaction has occurred in the process of mixing and printing. The sintered sample displayed absorption peaks caused by stretching vibration of the hydroxyl groups at 3442 cm^{-1} and adsorbed water and bound water molecules at 1637 cm^{-1} . Furthermore, there were peak observed at 590 cm^{-1} attributed to Al–O. These absorption peaks are consistent with the characteristic peaks of γ -Al₂O₃,³⁰ and they are in accordance with the results obtained from XRD analysis.

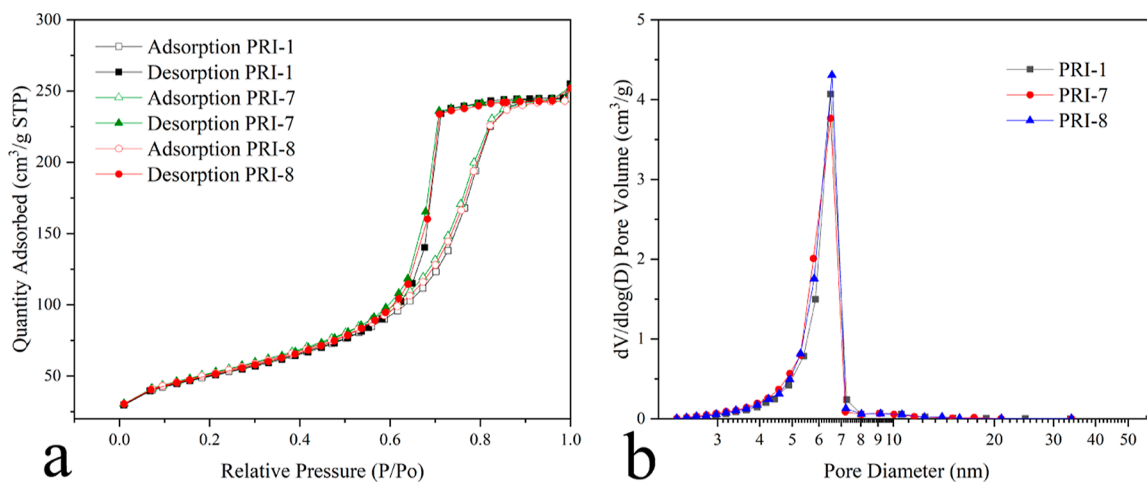
Effect of Three-Dimensional Printing Parameters on Mechanical Properties and Pore Structure under Orthogonal Conditions. An orthogonal test was conducted to examine the impact of 3D printing parameters on the

Table 2. Mechanical Properties and Pore Structure of Alumina Prepared via Orthogonal Experiments

samples	experimental factors			radial crushing strength (N/mm)	surface area (m ² /g)	pore volume (cm ³ /g)	pore diameter (nm)
	A/% (filling rate)	B/mm (nozzle diameter)	C/mm (layer thickness)				
PRI-1	1 (40)	1 (0.4)	1 (0.3)	4.95 ± 0.41	205.8847	0.380398	7.39051
PRI-2	1	2 (0.6)	2 (0.4)	7.12 ± 1.3	201.9501	0.381616	7.55862
PRI-3	1	3 (0.8)	3 (0.5)	6.13 ± 0.57	197.5993	0.384557	7.78458
PRI-4	2 (60)	1	2	17.17 ± 0.31	205.8955	0.378192	7.34726
PRI-5	2	2	3	21.95 ± 7.57	194.8041	0.382741	7.85900
PRI-6	2	3	1	32.44 ± 4.66	192.2614	0.367500	7.64584
PRI-7	3 (80)	1	3	42.93 ± 1.8	196.7172	0.381255	7.75235
PRI-8	3	2	1	48.07 ± 9.53	190.0723	0.381241	8.02307
PRI-9	3	3	2	47.13 ± 9.09	188.8056	0.385435	8.16575

Table 3. Results of Range Analysis

range	radial crushing strength			surface area			pore volume			pore diameter		
	A	B	C	A	B	C	A	B	C	A	B	C
K1	18.2	65.05	85.46	605.4341	608.4974	588.2184	1.146571	1.139845	1.129139	22.73371	22.49012	23.05942
K2	71.56	77.14	71.42	592.961	586.8265	596.6512	1.128433	1.145598	1.145243	22.8521	23.44069	23.07163
K3	138.13	85.7	71.01	575.5951	578.6663	589.1206	1.147931	1.137492	1.148553	23.94117	23.59617	23.39593
k1	6.07	21.68	28.49	201.8114	202.8325	196.0728	0.38219	0.379948	0.37638	7.5779	7.49671	7.68647
k2	23.85	25.71	23.81	197.6537	195.6088	198.8837	0.376144	0.381866	0.381748	7.61737	7.81356	7.69054
k3	46.04	28.57	23.67	191.865	192.8888	196.3735	0.382644	0.379164	0.382851	7.98039	7.86539	7.79864
R	39.97	6.89	4.82	9.9464	9.9437	2.8109	0.0065	0.002702	0.006471	0.40249	0.36868	0.11217

**Figure 9.** (a) Nitrogen physisorption isotherms and (b) pore size distributions of different alumina specimens.

mechanical properties and pore structure. The optimal Ink-3 formula setting was used in the experiment, and the consequences are presented in Table 2. The average value of the radial crushing strength of parallel samples in each test group was recorded as the mechanical performance at this factor level. Among all the samples, PRI-8 exhibited the highest radial crushing strength, measured at 48.07 ± 12.53 N/mm, while PRI-1 showed the lowest radial crushing strength at 4.95 ± 0.41 N/mm. PRI-4 exhibited the highest pore diameter of 7.34726 nm and surface area of 205.8955 m²/g, while PRI-9 showed the highest pore volume of 0.385435 cm³/g and lowest surface area of 188.8056 m²/g.

Range analysis of test data was carried out, and the consequences are presented in Table 3. In this experiment, the highest range value of factor A (filling rate) for the radial crushing strength of alumina specimens was 39.97, while the lowest range value belonged to factor C (layer thickness) at

4.82. The highest range value of factor A for the surface area of alumina specimens was 9.9464, while the lowest range value belonged to factor C at 2.8109. The highest range value of factor A for the pore volume of alumina specimens was 0.0065, while the lowest range value belonged to factor B at 0.002702. The highest range value of factor A for the pore diameter of alumina specimens was 0.40249, while the lowest range value belonged to factor C at 0.11217. It can be observed that factor A has the highest influence on the product performance.

The nitrogen physisorption isotherms of alumina specimens were classified as type IV isotherm, and hysteresis loop of H2 showed that alumina specimens have plentiful mesoporous structures (as displayed in Figure 9a).^{31,32} The pore diameter of alumina specimens was mostly in the range of 3–10 nm (as shown in Figure 9b), so the alumina specimens were mesoporous materials and could be well applied in catalytic reactions.^{33–36} There is little difference in the pore size

distribution and nitrogen physisorption isotherms of samples with three different printing parameters, which means the printing parameters hardly affect the pore properties of specimens. Therefore, the effect of printing factors on the sample strength is emphatically considered.

The influence of different levels of various factors on the radial crushing strength is illustrated in Figure 10. The radial

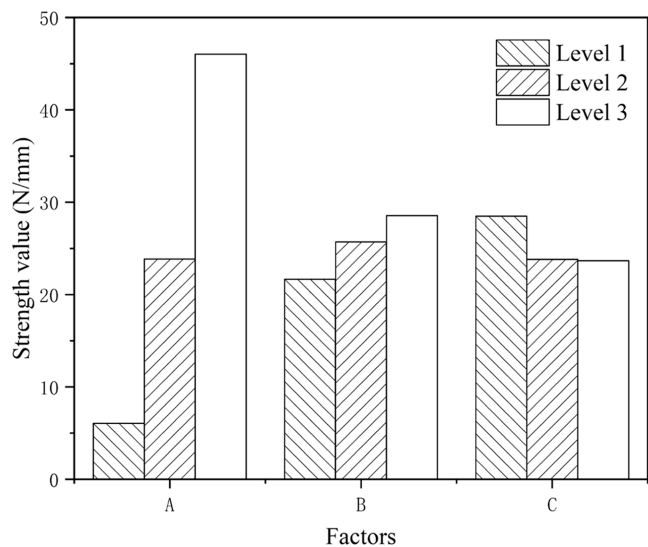


Figure 10. Influence of the printing parameter level on the radial crushing strength.

crushing strength increases with the increase in the filling rate and nozzle diameter. This indicates that as the filling rate and nozzle diameter increase, more lines with a larger diameter can better bear the radial force, resulting in higher sample strength. However, the radial crushing strength decreases with layer thickness increasing. This can be ascribed to the lower total height of the sample and weaker interaction between adjacent printed layers, leading to lower sample strength.

Figure 11 shows the microstructures of samples with different test numbers. In comparison to PRI-1, sample PRI-8, which had a higher filling amount, exhibited better layer adhesion, tighter lines, and a more complete structure. As a result, it was less prone to deformation and breakage under stress, allowing it to withstand greater forces. Similarly, when compared to PRI-7, PRI-8 characterized by a larger nozzle diameter and lower layer thickness exhibited wider lines, reduced interlayer height, smaller gaps, thicker lines, and higher sample density. Consequently, the radial crushing strength of PRI-8 was greater than that of PRI-7.

Figure 11b,d,f depicts the fractured sections of samples PRI-1, PRI-7, and PRI-8, respectively, at a magnification of 4000. Unlike PRI-7 and PRI-8, PRI-1 displayed noticeable cracks in the fractured section after being subjected to pressure crushing. This suggests that PRI-1 was more prone to breakage under stress, resulting in the lowest radial crushing strength.

CONCLUSIONS

In this paper, an alumina ink suitable for DIW 3D printing technology was prepared. Utilizing pseudoboehmite as the main component, Ink-3 containing 5 wt % nitric acid and 5 wt % sesbania powder demonstrated superior rheological properties, resulting in enhanced printability. Nine orthogonal experiments were designed using an orthogonal table of

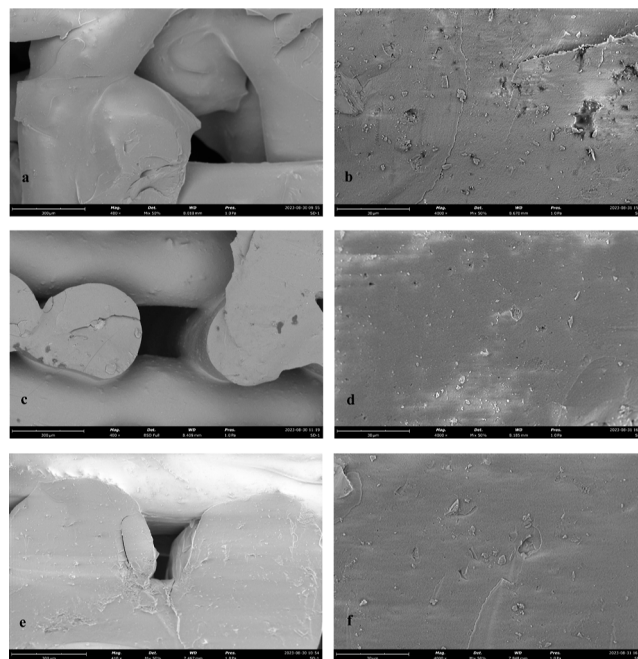


Figure 11. SEM images of samples (a,b) PRI-1, (c,d) PRI-7, and (e,f) PRI-8.

three factors and three levels to study the effects of filling ratio, nozzle diameter, and layer thickness on the performance of printed alumina. The results showed that the filling ratio had the greatest effect on the radial crushing strength of the specimens, followed by the nozzle diameter, while the layer thickness had the least influence. The surface areas of the samples were similar. Under the printing conditions of a filling rate of 80%, nozzle diameter of 0.6 mm, and layer thickness of 0.3 mm, sample PRI-8 exhibited the highest radial crushing strength of 48.07 N/mm and a surface area of 185.7315 m²/g.

AUTHOR INFORMATION

Corresponding Authors

Yanjuan Cui – College of Science, Institute of Agricultural Resources Chemistry and Application, Gansu Agricultural University, Lanzhou 730070, China; orcid.org/0000-0002-8636-7756; Email: cuiyanjun@gsau.edu.cn

Xiaoxin Chang – Lanzhou Petrochemical Research Center, Petrochemical Research Institute, Petrochina, Lanzhou 730060, China; Email: changxiaoxin@petrochina.com.cn

Authors

Shuo Wang – College of Science, Institute of Agricultural Resources Chemistry and Application, Gansu Agricultural University, Lanzhou 730070, China

Yongsheng Xiang – Lanzhou Petrochemical Research Center, Petrochemical Research Institute, Petrochina, Lanzhou 730060, China

Hui Feng – College of Science, Institute of Agricultural Resources Chemistry and Application, Gansu Agricultural University, Lanzhou 730070, China

Xiaofei Liu – Lanzhou Petrochemical Research Center, Petrochemical Research Institute, Petrochina, Lanzhou 730060, China

Jinxu Guo – College of Science, Institute of Agricultural Resources Chemistry and Application, Gansu Agricultural University, Lanzhou 730070, China

Peng Tu – College of Science, Institute of Agricultural Resources Chemistry and Application, Gansu Agricultural University, Lanzhou 730070, China

Complete contact information is available at:
<https://pubs.acs.org/10.1021/acsomega.4c00819>

Notes

The authors declare no competing financial interest.

ACKNOWLEDGMENTS

We acknowledge the financial support from the Scientific research start-up funds for openly recruited doctors provided by Gansu Agricultural University #1 (GAU-KYQD-2019-24), the Youth Science and Technology Fund Program in Gansu Province #2 of China (22JR5RA888), and the Natural Science Basic Research Plan in Shaanxi Province #3 of China (2020JQ-119).

REFERENCES

- (1) Karouia, F.; Boualleg, M.; Digne, M.; Alphonse, P. Control of the textural properties of nanocrystalline boehmite (γ -AlOOH) regarding its peptization ability. *Powder Technol.* **2013**, *237*, 602–609.
- (2) Zhang, Y.; Lv, Y.; Mo, Y.; Li, H.; Tang, P.; Li, D.; Feng, Y. Facile Preparation and Promising Hydrothermal Stability of Spherical γ -Alumina Support with High Specific Surface Area. *Catalysts* **2022**, *12* (11), 1416.
- (3) Islam, A.; Taufiq-Yap, Y. H.; Ravindra, P.; Teo, S. H.; Sivasangar, S.; Chan, E.-S. Biodiesel synthesis over millimetric γ -Al₂O₃/KI catalyst. *ENERGY*. **2015**, *89*, 965–973.
- (4) Pype, J.; Michielsen, B.; Seftel, E. M.; Mullens, S.; Meynen, V. Development of alumina microspheres with controlled size and shape by vibrational droplet coagulation. *J. Eur. Ceram. Soc.* **2017**, *37* (1), 189–198.
- (5) Falkowski, P.; Zurowski, R. Shaping of alumina microbeads by drop-casting of the photopolymerizable suspension into silicone oil and UV curing. *J. Eur. Ceram. Soc.* **2022**, *42* (9), 3957–3967.
- (6) Garbarino, G.; Kowalik, P.; Riani, P.; Antoniak-Jurak, K.; Pieta, P.; Lewalska-Graczyk, A.; Lisowski, W.; Nowakowski, R.; Busca, G.; Pieta, I. S. Improvement of Ni/Al₂O₃ CATALYSTS for Low-Temperature CO₂Methanation by Vanadium and Calcium Oxide Addition. *Ind. Eng. Chem. Res.* **2021**, *60* (18), 6554–6564.
- (7) Hossain, S. S.; Lu, K. Recent progress of alumina ceramics by direct ink writing: Ink design, printing and post-processing. *Ceram. Int.* **2023**, *49* (7), 10199–10212.
- (8) Saadi, M. A. S. R.; Maguire, A.; Pottackal, N. T.; Thakur, M. S. H.; Ikram, M. M.; Hart, A. J.; Ajayan, P. M.; Rahman, M. M. Direct Ink Writing: A 3D Printing Technology for Diverse Materials. *Adv. Mater.* **2022**, *34* (28), 2108855.
- (9) Feng, J.; Su, B.-L.; Xia, H.; Zhao, S.; Gao, C.; Wang, L.; Ogbeide, O.; Feng, J.; Hasan, T. Printed aerogels: chemistry, processing, and applications. *Chem. Soc. Rev.* **2021**, *50* (6), 3842–3888.
- (10) Zhu, J.; Wu, P.; Chao, Y.; Yu, J.; Zhu, W.; Liu, Z.; Xu, C. Recent advances in 3D printing for catalytic applications. *Chem. Eng. J.* **2022**, *433*, 134341.
- (11) Chan, S. S. L.; Sesso, M. L.; Franks, G. V. Direct ink writing of hierarchical porous alumina-stabilized emulsions: Rheology and printability. *J. Am. Ceram. Soc.* **2020**, *103* (10), 5554–5566.
- (12) Chen, A.-N.; Li, M.; Xu, J.; Lou, C.-H.; Wu, J.-M.; Cheng, L.-J.; Shi, Y.-S.; Li, C.-H. High-porosity mullite ceramic foams prepared by selective laser sintering using fly ash hollow spheres as raw materials. *J. Eur. Ceram. Soc.* **2018**, *38* (13), 4553–4559.
- (13) He, R.; Ding, G.; Zhang, K.; Li, Y.; Fang, D. Fabrication of SiC ceramic architectures using stereolithography combined with precursor infiltration and pyrolysis. *Ceram. Int.* **2019**, *45* (11), 14006–14014.
- (14) Sun, Y.; Li, M.; Jiang, Y.; Xing, B.; Shen, M.; Cao, C.; Wang, C.; Zhao, Z. High-Quality Translucent Alumina Ceramic Through Digital Light Processing Stereolithography Method. *Adv. Eng. Mater.* **2021**, *23* (7), 2001475.
- (15) Chen, Z.; Li, Z.; Li, J.; Liu, C.; Lao, C.; Fu, Y.; Liu, C.; Li, Y.; Wang, P.; He, Y. 3D printing of ceramics: A review. *J. Eur. Ceram. Soc.* **2019**, *39* (4), 661–687.
- (16) Coppola, B.; Tardivat, C.; Richaud, S.; Tulliani, J.-M.; Montanaro, L.; Palmero, P. 3D printing of dense and porous alkali-activated refractory wastes via Direct Ink Writing (DIW). *J. Eur. Ceram. Soc.* **2021**, *41* (6), 3798–3808.
- (17) Shahzad, A.; Lazoglu, I. Direct ink writing (DIW) of structural and functional ceramics: Recent achievements and future challenges. *Composites, Part B* **2021**, *225*, 109249.
- (18) Jiang, Z.; Erol, O.; Chatterjee, D.; Xu, W.; Hibino, N.; Romer, L. H.; Kang, S. H.; Gracias, D. H. Direct Ink Writing of Poly(tetrafluoroethylene) (PTFE) with Tunable Mechanical Properties. *ACS Appl. Mater. Interfaces* **2019**, *11* (31), 28289–28295.
- (19) Armstrong, C. D.; Yue, L.; Deng, Y.; Qi, J. Enabling direct ink write edible 3D printing of food purees with cellulose nanocrystals. *J. Food Eng.* **2022**, *330*, 111086.
- (20) Xu, C.; Ban, M.; Zhang, H.; Liu, Q.; Ren, L. Direct ink writing of porous Fe-HA metal-matrix composites (MMCs) with independently adjustable porosity and degradation rate for bone implant applications. *Mater. Des.* **2022**, *224*, 111319.
- (21) Yang, G.; Guan, R.; Zhen, H.; Ou, K.; Fang, J.; Li, D.-S.; Fu, Q.; Sun, Y. Tunable Size of Hierarchically Porous Alumina Ceramics Based on DIW 3D Printing Supramolecular Gel. *ACS Appl. Mater. Interfaces* **2022**, *14* (8), 10998–11005.
- (22) Rane, K.; Farid, M. A.; Hassan, W.; Strano, M. Effect of printing parameters on mechanical properties of extrusion-based additively manufactured ceramic parts. *Ceram. Int.* **2021**, *47* (9), 12189–12198.
- (23) Liu, N.; Sun, X.; Chen, Z.; Xu, Z.; Dai, N.; Shi, G.; Cai, S.; Lv, X.; Zheng, C. Direct ink writing of dense alumina ceramics prepared by rapid sintering. *Ceram. Int.* **2022**, *48* (20), 30767–30778.
- (24) Yang, L.; Zeng, X.; Zhang, Y. 3D printing of alumina ceramic parts by heat-induced solidification with carrageenan. *Mater. Lett.* **2019**, *255*, 126564.
- (25) del-Mazo-Barbara, L.; Ginebra, M.-P. Rheological characterisation of ceramic inks for 3D direct ink writing: A review. *J. Eur. Ceram. Soc.* **2021**, *41* (16), 18–33.
- (26) Outrequin, T. C. R.; Gamonpilas, C.; Siriawatwechakul, W.; Sreearunothai, P. Extrusion-based 3D printing of food biopolymers: A highlight on the important rheological parameters to reach printability. *J. Food Eng.* **2023**, *342*, 111371.
- (27) Chan, S. S. L.; Pennings, R. M.; Edwards, L.; Franks, G. V. 3D printing of clay for decorative architectural applications: Effect of solids volume fraction on rheology and printability. *Addit. Manuf.* **2020**, *35*, 101335.
- (28) Ye, Z.; Chu, C.; Zhang, D.; Ma, S.; Guo, J.; Cheng, Y.; Xu, G.; Li, Z.; Sun, A. Study on 3D-Direct Ink Writing based on adding silica submicron-particles to improve the rheological properties of alumina ceramic ink. *Mater. Today Commun.* **2021**, *28*, 102534.
- (29) Jagtap, S.; Yenkie, M. K. N.; Labhsetwar, N.; Rayalu, S. Defluorination of drinking water using chitosan based mesoporous alumina. *Microporous Mesoporous Mater.* **2011**, *142* (2–3), 454–463.
- (30) Li, G.; Liu, Y.; Tang, Z.; Liu, C. Effects of rehydration of alumina on its structural properties, surface acidity, and HDN activity of quinoline. *Appl. Catal., A* **2012**, *437–438*, 79–89.
- (31) Bui, H. M.; Fischer, R.; Szesni, N.; Tonigold, M.; Achterhold, K.; Pfeiffer, F.; Hinrichsen, O. Development of a manufacturing process for Binder Jet 3D printed porous Al₂O₃ supports used in heterogeneous catalysis. *Addit. Manuf.* **2022**, *50*, 102498.
- (32) Huo, C.; Tian, X.; Chen, C.; Zhang, J.; Nan, Y.; Zhong, Q.; Huang, X.; Hu, J.; Li, D. Hierarchically porous alumina catalyst carrier with biomimetic vein structure prepared by direct ink writing. *J. Eur. Ceram. Soc.* **2021**, *41* (7), 4231–4241.
- (33) Hurt, C.; Brandt, M.; Priya, S. S.; Bhatelia, T.; Patel, J.; Selvakannan, P. R.; Bhargava, S. Combining additive manufacturing and catalysis: a review. *Catal. Sci. Technol.* **2017**, *7* (16), 3421–3439.

- (34) Liu, D.; Zou, D.; Zhu, H.; Zhang, J. Mesoporous Metal–Organic Frameworks: Synthetic Strategies and Emerging Applications. *Small* **2018**, *14* (37), 1801454.
- (35) Pradeep, N.; Sastry, C. C.; Brandao, L.; Meennakshi, B. S. 3D Printing of Shrimp Derived Chitosan with HAp as a Bio-Composite Scaffold. *Mater. Manuf. Processes* **2022**, *37* (11), 1257–1266.
- (36) Wang, Y.-Z.; Zhang, L.-Y.; Mo, Y.; Wei, G.-T.; Li, Z.-M.; Huang, K.; Deng, Y. Preparation of a Low-Cost Adsorption Material from Red Mud and Bagasse. *Mater. Manuf. Processes* **2016**, *31* (2), 162–167.